J Appl Electrochem (2012) 42:629–643
DOI 10.1007/s10800-012-0447-8

ORIGINAL PAPER

Electrochemical recovery of nickel from nickel sulfamate plating effluents

A. Hankin · G. H. Kelsall

Received: 16 February 2012 / Accepted: 3 July 2012 / Published online: 27 July 2012

Abstract Nickel sulfamate solutions are widely used for industrial nickel plating, when electrodeposits with low stress are required. Partial decomposition of sulfamate with decreasing pH below ca. 2.5 degrades the properties of nickel electrodeposits, decreases the charge yield and results in spent solutions, from which nickel must be recovered before they could be discharged to sewers. Results are reported of charge yields for nickel recovery from an industrial sulfamate effluent, using an electrochemical reactor operated at constant current in batch-recycle mode and incorporating a nickel mesh cathode, a $Ti/Ta_2O_5–IrO_2$ mesh anode and a cation-permeable membrane to prevent anodic oxidation of sulfamate. A micro-kinetic model was developed, treating the processes of nickel(II) and proton reduction in sulfamate solutions as two multi-step reactions involving adsorbed intermediates, Ni^I_{ads} and H_{ads}, respectively. The unknown kinetic parameters were obtained using *gPROMS* software by iterative fitting of the model to experimental data obtained over a range of nickel(II) concentrations and bulk solution pH, enabling evaluation of nickel(II) reduction charge yields as a function of nickel(II) concentration, bulk pH and electrode potential. A model combining the micro-kinetic equations with mass and charge balances on the reactor was used to determine the control parameters for electrochemical recovery of elemental metal from nickel(II) in batch-recycle mode. It was determined experimentally that a decrease in catholyte pH to values below ca. 2.5 resulted in a decrease in nickel(II) reduction charge yields to values below 0.9. The decrease in catholyte pH, caused by the flux of protons from the anolyte where they were generated via anodic oxygen evolution, was obviated by continuous addition of NaOH at a rate determined by the model, permitting nickel(II) recovery with an average charge yield of 0.94.

Keywords Nickel · Sulfamate · Electrodeposition · Effluents · Waste water · Kinetic model

List of Symbols

A	Area (m^2)
C	Concentration (mol m^{-3})
C_f	Sensitivity coefficient of an EQCM (ng Hz^{-1})
D	Diffusion coefficient (m^2 s^{-1})
E	Electrode potential (V)
f	Frequency (Hz)
F	Faraday constant (C mol^{-1})
I	Current (A)
j	Current density (A m^{-2})
j_L	Mass transport limited current density (A m^{-2})
k	Kinetic rate coefficient (m s^{-1} or s^{-1})
k_m	Mass transport rate constant (m s^{-1})
K	Equilibrium constant (1)
m	Mass (kg)
M	Molar mass (g mol^{-1})
Q	Electric charge (C)
R	Universal gas constant (J mol^{-1} K^{-1})
t	Time (s) or (h)
T	Temperature (K)
U	Cell voltage (V)
V	Volume (m^3)
w^e	Specific electrical energy consumption (kW h)
α	Transfer coefficient (1)
β	Tafel slope (mV dec^{-1})
Γ	Surface concentration (mol m^{-2})
η	Reaction overpotential (V)
θ_{ads}	Fractional surface coverage by adsorbed species (1)

A. Hankin · G. H. Kelsall (✉)
Department of Chemical Engineering, Imperial College London, South Kensington, London SW 7 2AZ, UK
e-mail: g.kelsall@imperial.ac.uk

v Kinetic rate (mol m^{-2} s^{-1})
v_e Electron stoichiometry (1)
ξ Electro-osmotic drag coefficient (1)
ρ Density (g cm^{-3})
Φ^e Fractional charge yield (1)

1 Introduction

Aqueous nickel(II) sulfamate (amidosulfonate) solutions are used widely in industrial surface finishing processes for electrodeposition of nickel. Nickel sulfamate plating baths typically contain 300–450 kg m^{-3} nickel sulfamate, 0–30 kg m^{-3} nickel chloride and 30–45 kg m^{-3} boric acid [1] and generate electrodeposits with low stress at high charge yields.

The finite lifetimes of nickel sulfamate plating baths are caused by the tendency of the sulfamate ions to hydrolyse to ammonium and sulfate ions at bath operating conditions of pH below 2.5 and temperatures above 65 °C [2] via:

$$NH_2SO_3^- + H^+ + H_2O \rightarrow NH_4^+ + HSO_4^- \quad (1)$$

The accumulation of ammonium ions in the plating bath increases stress in nickel electrodeposits [3], so high sulfamate hydrolysis rates eventually render the plating solutions unusable for production of high quality deposits. This results in large volumes of toxic spent solutions containing $>10^3$ mol Ni^{II} m^{-3}, whereas consent concentrations for discharge to sewers are typically $<10^{-2}$ mol m^{-3}. The spent solutions thus require treatment to recover nickel in order to enable disposal into the environment.

Electrochemical recovery of nickel in elemental form from the aqueous effluents is motivated by the current price of nickel of ca. $ 17 k tonne^{-1} (www.lme.com), which is two orders of magnitude greater than the likely running costs of an electrochemical reactor, dominated by specific electrical energy consumptions:

$$w^e_{Ni} \text{ / kWh (tonne Ni)}^{-1} = \frac{2F}{\Phi^e_{Ni}} \cdot \frac{U}{3.6M_{Ni}} \cong 913\frac{U}{\Phi^e_{Ni}} \quad (2)$$

where U is the cell voltage across the reactor at the operating current density, Φ^e_{Ni} the fractional charge yield for Ni^{II} reduction and M_{Ni} the molar mass of Ni.

The objectives of the presently reported research were:

- to establish optimum operating conditions and control methods for the recovery of nickel(II) from nickel sulfamate effluents in a bench scale reactor;
- to develop a micro-kinetic model to predict the kinetics of nickel sulfamate effluent reduction, based on the bulk nickel(II) concentration and pH;
- to couple the micro-kinetic model with the macro-scale reactor model to predict optimal operating conditions.

Although much has been published on the various macroscopic properties of deposits obtained from nickel sulfamate plating baths [3–5], there is an absence of reports on nickel(II) recovery from sulfamate effluent solutions or on modelling the kinetics of such processes.

1.1 Process chemistry

Table 1 lists the composition of several samples of nickel sulfamate effluents from an industrial source. The effluents were analysed using a variety of techniques and were found to consist primarily of nickel(II) and boric acid, while contaminants included ammonium and sulfate ions, the products of sulfamate hydrolysis, as well as dissolved iron. Ion chromatography provided no evidence for the presence in these particular effluents of chloride ions, which are often added to depassivate nickel anodes during plating. The chemical analysis results in Table 1 were corroborated by external analysis conducted at the effluent source.

Figure 1 shows the effect of pH on the speciation of nickel(II) in the nickel sulfamate effluents, determined computationally from equilibrium constants listed in Eqs. (3–12): (3–5) [6], (6–10) [7] and (11–12) [8]. As no references were found to the contrary, it was assumed that nickel(II) does not form aqueous complexes with sulfamate ions, $NH_2SO_3^-$, which thus were excluded from the nickel(II) speciation calculations.

$$Ni^{2+} + 2H_2O \rightleftarrows Ni(OH)_2(c) + 2H^+; \quad K = 1.87 \times 10^{-13} \quad (3)$$

$$Ni^{2+} + 2H_2O \rightleftarrows Ni(OH)_2(aq) + 2H^+; \quad K = 1.07 \times 10^{-28} \quad (4)$$

$$Ni^{2+} + H_2O \rightleftarrows NiOH^+ + H^+; \quad K = 2.20 \times 10^{-10} \quad (5)$$

$$HSO_4^- \rightleftarrows SO_4^{2-} + H^+; \quad K = 1.01 \times 10^{-2} \quad (6)$$

$$Ni^{2+} + SO_4^{2-} \rightleftarrows NiSO_4(aq); \quad K = 5.89 \times 10^{-3} \quad (7)$$

$$NH_4^+ \rightleftarrows NH_3 + H^+; \quad K = 5.61 \times 10^{-10} \quad (8)$$

$$Ni(OH)_2(c) + 4NH_4^+ \rightleftarrows Ni(NH_3)_4^{2+} + 2H^+ + 2H_2O; \quad K = 5.50 \times 10^{-19} \quad (9)$$

Table 1 Ionic content of a set of industrial nickel sulfamate plating effluents

Species	Concentration (mol m^{-3})	Method of analysis
Ni^{II}	700–2,500	ICP
Fe^{II} or Fe^{III}	0.8–6.5	ICP
$B(OH)_3$	ca. 190	XRF
SO_4^{2-}	ca. 100	IC
NH_4^+	ca. 270	IC
$[H^+]$	$(10^{-1.8}–10^{-4.5}) \times 10^3$	pH meter

$$Ni(OH)_2(c) + 6NH_3 + 2H^+ \rightleftarrows Ni(NH_3)_6^{2+} + 2H_2O;\quad K = 3.64 \times 10^{19} \tag{10}$$

$$B(OH)_3 \rightleftarrows H^+ + BO(OH)_2^-;\quad K = 1.00 \times 10^{-8} \tag{11}$$

$$Ni^{2+} + 2BO(OH)_2^- \rightleftarrows Ni[BO(OH)_2]_2;\quad K = 10^{3.8} \tag{12}$$

Figure 1 shows that in the nickel sulfamate effluents, nickel(II) is soluble in the acidic pH range and is present predominantly as free Ni^{2+} ions. A proportion of free Ni^{2+} is complexed by sulfate ions, forming aqueous $NiSO_4$, while much smaller proportions are complexed by hydroxide ions and monoborate ions, forming $NiOH^+$ and $Ni[BO(OH)_2]_2$ complexes, respectively. At pH above ca. 6, nickel(II) is predominantly present as insoluble crystalline $Ni(OH)_2(c)$. The activity of $Ni(OH)_2(aq)$ was predicted to be negligibly small, so it may be disregarded. At neutral/alkaline pHs, small proportions of $Ni(OH)_2(c)$ are complexed by NH_4^+ ions and NH_3 molecules, forming the $Ni(NH_3)_4^{2+}$ and $Ni(NH_3)_6^{2+}$ aqueous compounds, respectively.

1.2 Process electrochemistry

1.2.1 Cathodic reactions

Based on the speciation diagram in Fig. 1, the overall reaction at the cathode is nominally:

$$Ni^{2+} + 2e^- \rightarrow Ni$$

$$\text{At } 298\,\text{K}:\quad E_{Ni^{2+}/Ni^0}(\text{SCE})/V = -0.4855 + 0.0296\log(Ni^{2+}) \tag{13}$$

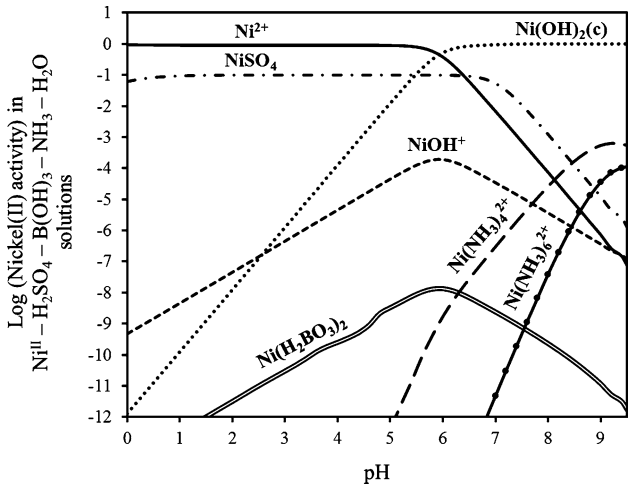

Fig. 1 Thermodynamically predicted speciation of an aqueous Ni^{II}–NH_3SO_3–$B(OH)_3$–H_2SO_4–NH_3–H_2O system based on concentrations which reflect the typical effluent content: $[Ni^{II}] = 1$ M, $[B(OH)_3] = 0.19$ M, $H_2SO_4 = 0.1$ M and $NH_3 = 0.27$ M

though the detail of the reaction mechanism for nickel deposition has yet to be established unambiguously. Hydrogen evolution is a parallel loss reaction by the reduction of protons:

$$2H^+ + 2e^- \rightarrow H_2$$

$$\text{At } 298\,\text{K}:\quad E_{H^+/H_2}(\text{SCE})/V = -0.245 - 0.0592\text{pH} - 0.0296\log(p_{H_2}) \tag{14}$$

coinciding with the kinetic and mixed control regions of Ni^{II} reduction, and by the reduction of water:

$$2H_2O + 2e^- \rightarrow H_2 + 2OH^- \tag{15}$$

which typically occurs at more negative electrode potentials, coinciding with the mass transport controlled Ni^{II} reduction. Both reactions decrease the Ni^{II} reduction charge yield, Φ^e_{Ni}. The additional decrease in Φ^e_{Ni} due to the reduction of oxygen via (16) can be minimised by purging the solution vigorously with N_2 gas:

$$O_2 + 4H^+ + 4e^- \rightarrow 2H_2O \tag{16}$$

1.2.2 Anodic reactions

In contrast to industrial plating processes, during which nickel anodes dissolve to replenish the Ni^{II} ions consumed at the cathode, IrO_2–Ta_2O_5 coated titanium-based anodes may be utilised instead during electrochemical recovery of nickel(II) from effluents, resulting in the primary anodic reaction (17):

$$O_2 + 4H^+ + 4e^- \leftarrow 2H_2O \tag{17}$$

In addition to the anodic evolution of oxygen, direct oxidation of the sulfamate ion has been proposed [9–13]. It has been demonstrated experimentally that the oxidation of the amino group in sulfamate ions may occur at such anodes, the proposed oxidation products being N_2 gas and SO_3^{2-} [9] as well as $N_2H_2(SO_3)_2^{2-}$, $N_2(SO_3)_2^{2-}$, $S_2O_8^{2-}$ [11], depending on the anode potential.

Based on the published literature, it is certain that some of the anodic sulfamate oxidation products affect the Ni electrodeposits, giving rise to changes in stress and brightness. However, it is not clear whether the nickel charge yield is affected and what the long term effects of sulfamate oxidation product accumulation would be on the nickel deposits. As a precaution, a cation-permeable membrane was used to isolate the nickel sulfamate liquor from the anode, preventing the migrational transport of $NH_2SO_3^-$ into the anolyte and constraining the anodic reaction to the evolution of O_2 via reaction (17).

2 Model formulations

2.1 Micro-kinetic model of reaction mechanisms

A model was formulated describing the combined micro-kinetics of nickel(II) and proton reduction, which were each treated as multi-step reactions involving adsorbed intermediates [14–16]. The objective of the model was to define the effects of electrode potential, nickel(II) concentration and pH on the rates of nickel(II) reduction. Based on the effluent speciation shown in Fig. 1, changes in the charge yield, Φ^{e}_{Ni}, during electrochemical treatment of nickel sulfamate effluents will be determined predominantly by the extent of competition from the H_2 evolution reactions (14) and (15).

The following assumptions were made in constructing the rate equations:

1. Both adsorbates follow Langmuir isotherms;
2. Reaction mechanisms are not pH dependent at acidic pHs;
3. Transfer coefficients do not change with potential;
4. Migration fluxes in the interfacial region can be neglected because of the presence of excess supporting electrolyte;
5. No homogeneous reactions occur within the interfacial boundary layer.

When a solute reactant, A, is reduced to an adsorbate, B, the rate equation representing the processes of adsorption during reduction and desorption during oxidation is given in (18)

$$\frac{j}{F} = -k_{\mathrm{c,ads}}[A]_{\mathrm{sol}}(1-\theta_B)\exp\left\{-\frac{\alpha F\eta}{RT}\right\} + k_{\mathrm{a,des}}\Gamma_{\mathrm{max},B}\theta_B\exp\left\{\frac{(1-\alpha)F\eta}{RT}\right\} \quad (18)$$

where $k_{\mathrm{c,ads}}$ and $k_{\mathrm{a,des}}$ are the rates of adsorption and desorption, respectively, θ_B is the fractional surface coverage by bound species, B, $\Gamma_{\mathrm{max},B}$ is the maximum surface concentration of B, α is the transfer coefficient and η is the reaction overpotential.

Equation (19) was used to describe the reduction kinetics of individual electron transfer steps, with kinetic coefficients k_{c}, which were expected to be subject to mass transport limitation, with coefficient k_{m}:

$$v_{\mathrm{C}} \propto \frac{k_{\mathrm{c}}\exp\left\{-\frac{\alpha F\eta}{RT}\right\}}{\left(1+\frac{k_{\mathrm{c}}}{k_{\mathrm{m}}}\exp\left\{-\frac{\alpha F\eta}{RT}\right\}\right)} \quad (19)$$

2.1.1 Micro-kinetic model of proton reduction

The proton reduction mechanism is modelled on the Volmer–Heyrovsky and the Volmer–Tafel mechanisms operating simultaneously, with mass transport limitation applying to the Volmer step. H_2 evolution was modelled as proceeding via an adsorbed intermediate, H_{ads}, occupying a fraction θ_{H} of the electrode surface area. In the following rate equations, η_{H} represents the reaction overpotential relative to the equilibrium potential for the H^+/H_2 couple; the potential differences $\left(E_{H^+/H_2} - E_{H^+/H_{\mathrm{ads}}}\right)$ and $\left(E_{H^+/H_2} - E_{H_{\mathrm{ads}}/H_2}\right)$ are contained within the respective kinetic rate coefficients. v_{c} and v_{a} represent the cathodic and anodic kinetic rates, respectively; the fraction of the electrode surface area on which adsorption can take place is that unoccupied by either adsorbed hydrogen, θ_{H}, or nickel, θ_{Ni}, intermediates. θ_{Ni} is zero in the absence of nickel(II) in solution.

The Volmer step (reversible):

$$\mathrm{H}^+ + e^- \underset{v_{V_{\mathrm{a}}}}{\overset{v_{V_{\mathrm{c}}}}{\rightleftarrows}} H^{\theta_{\mathrm{H}}}_{(\mathrm{ads})} \quad (20)$$

$$v_{V_{\mathrm{c}}} = \frac{k_{V_{\mathrm{c}}}\exp\left\{-\frac{\alpha_V F\eta_{\mathrm{H}}}{RT}\right\}}{\left[1+\frac{k_{V_{\mathrm{c}}}}{k_{\mathrm{m,H^+}}}\exp\left\{-\frac{\alpha_V F\eta_{\mathrm{H}}}{RT}\right\}\right]}[\mathrm{H}^+](1-\theta_{\mathrm{H}}-\theta_{\mathrm{Ni}}) \quad (21)$$

$$v_{V_{\mathrm{a}}} = k_{V_{\mathrm{a}}}\Gamma_{\mathrm{H,max}}\theta_{\mathrm{H}}\exp\left\{\frac{(1-\alpha_V)F\eta_{\mathrm{H}}}{RT}\right\} \quad (22)$$

The Heyrovsky step (irreversible):

$$[\mathrm{H}]^{\theta_{\mathrm{H}}}_{(\mathrm{ads})} + \mathrm{H}^+_{(\mathrm{aq})} + e^- \xrightarrow{v_{\mathrm{Hc}}} H_{2(\mathrm{aq})} \quad (23)$$

$$v_{\mathrm{H_c}} = k_{\mathrm{H_c}}[\mathrm{H}^+]\theta_{\mathrm{H}}\exp\left\{-\frac{\alpha_{\mathrm{H}}F\eta_{\mathrm{H}}}{RT}\right\} \quad (24)$$

The Tafel step (irreversible):

$$[\mathrm{H}]^{\theta_{\mathrm{H}}}_{(\mathrm{ads})} + [\mathrm{H}]^{\theta_{\mathrm{H}}}_{(\mathrm{ads})} \xrightarrow{v_T} \mathrm{H}_{2(\mathrm{aq})} \quad (25)$$

$$v_{\mathrm{T}} = k_{\mathrm{T}}\Gamma_{\mathrm{H,max}}\theta^2_{\mathrm{H}} \quad (26)$$

2.1.2 Micro-kinetic model of nickel(II) reduction

The most widely accepted mechanism for the reduction of nickel(II) and other iron group metals proposes that the kinetics increase with increasing pH due to hydrolysis of Ni^{2+} ions to $NiOH^+$ ions, which are reported as then becoming the primary reactant. In most publications supporting this hypothesis [17, 18], nickel speciation is calculated without account for $Ni(OH)_2$ formation, leading to the computation of erroneously high $NiOH^+$ concentrations. Once $Ni(OH)_2$ is taken into account, as shown in the speciation diagram in Fig. 1, it is evident that $NiOH^+$ is present in such small quantities relative to Ni^{2+} that it is unlikely to contribute to the reduction kinetics at any pH and so this hypothesis is not supported here.

It is asserted that the only way in which the nickel(II) and proton reduction reactions are coupled is via competition for adsorption sites between adsorbed hydrogen, θ_H, and adsorbed nickel(I), $\theta_{Ni(I)}$, on the electrode surface area. Beyond the competition for surface sites and in the absence of the $Ni(OH)_2$ precipitation via reaction (3), the solution pH is assumed not to have an effect on the kinetics of nickel(II) reduction. In the proposed rate equations for nickel(II) reduction, η_{Ni} represents the reaction overpotential relative to the equilibrium potential for the Ni^{2+}/Ni^0 couple; the potential differences $\left(E_{Ni^{2+}/Ni^0} - E_{Ni^{2+}/Ni^I_{ads}}\right)$ and $\left(E_{Ni^{2+}/Ni^0} - E_{Ni^I_{ads}/Ni^0}\right)$ are contained within the relevant kinetic rate coefficients.

The first electron transfer (reversible):

$$\left(Ni^{2+}\right)_{aq} + e^- \underset{\nu_{Ni,a1}}{\overset{\nu_{Ni,c1}}{\rightleftarrows}} \left[Ni^I\right]^{\theta_{Ni}}_{(ads)} \tag{27}$$

$$\nu_{Ni,c1} = \frac{k_{Ni,c1}\exp\left\{-\frac{\alpha_{Ni,1}F\eta_{Ni}}{RT}\right\}}{\left(1 + \frac{k_{Ni,c1}}{k_{m,Ni^{II}}}\exp\left\{-\frac{\alpha_{Ni,1}F\eta_{Ni}}{RT}\right\}\right)}\left[Ni^{II}\right](1 - \theta_H - \theta_{Ni}) \tag{28}$$

$$\nu_{Ni,a1} = k_{Ni,a1}\Gamma_{Ni,max}\theta_{Ni}\exp\left\{\frac{(1-\alpha_{Ni,1})F\eta_{Ni}}{RT}\right\} \tag{29}$$

The second electron transfer step (irreversible):

$$\left[Ni^I\right]^{\theta_{Ni}}_{(ads)} + e^- \xrightarrow{\nu_{Ni,c2}} Ni \tag{30}$$

$$\nu_{Ni,c2} = k_{Ni,c2}\Gamma_{Ni,max}\theta_{Ni}\exp\left\{-\frac{\alpha_{Ni,2}F\eta_{Ni}}{RT}\right\} \tag{31}$$

Mass balances on adsorbates H_{ads} and Ni^I_{ads} in the steady state:

$$\Gamma_{H,max}\frac{d\theta_H}{dt} = \nu_{V_c} - \nu_{V_a} - \nu_{H_c} - \nu_T \tag{32}$$

$$\Gamma_{Ni,max}\frac{d\theta_{Ni}}{dt} = \nu_{Ni,c1} - \nu_{Ni,a1} - \nu_{Ni,c2} \tag{33}$$

Charge balances:

$$j_{H_2} = -F(\nu_{V_c} - \nu_{V_a} + \nu_{H_c}) \tag{34}$$

$$j_{Ni} = -F(\nu_{Ni,c1} - \nu_{Ni,a1} + \nu_{Ni,c2}) \tag{35}$$

$$j_{total} = j_{H_2} + j_{Ni} \tag{36}$$

While the aim was to measure and model the kinetics of nickel(II) reduction from a nickel sulfamate effluent, initial kinetic investigations were performed with ultrapure synthetic solutions not containing ammonium and iron contaminants typical of such spent plating baths. However, boric acid was retained as a component in the synthetic solutions to prevent nickel(II) passivation by reaction (3) and the consequent degradation of the deposit; in the absence of boric acid, passivation during plating has been reported to occur at bulk solution pHs as low as 3.5 [19]. Boric acid has also been reported to modify both the H_2 evolution [16, 20, 21] and nickel(II) reduction kinetics [22, 23]; however, a priori inclusion of its effects in the model are excluded.

2.2 Electrochemical reactor model

To achieve a substantial degree of depletion in nickel(II) concentration in effluent samples, a membrane-divided electrochemical reactor was operated in batch-recycle mode, as shown schematically in Fig. 2. The nickel sulfamate effluent was used as the catholyte and aqueous sodium sulfate electrolyte as the anolyte.

The assumptions made in the construction of mass balance equations representing reactor processes:

1. Catholyte and anolyte reservoirs are perfectly mixed; electrolyte volumes contained in the reactor compartment and in the reservoir at any time are treated additively as a unified volume to which mass balance equations apply.
2. Conversion per pass is low (ca. 0.11 % based on plug flow considerations [24] and assuming a charge yield of unity in the concentration range studied here). Hence the concentration changes between reactor inlet and outlet could be neglected to a first approximation.
3. Ionic transport in the reactor occurs by convective diffusion only.
4. The mass transfer coefficient is constant throughout the reactor.
5. The catholyte pH is always higher than the anolyte pH.
6. Diffusional fluxes between compartments are negligible relative to migrational fluxes.

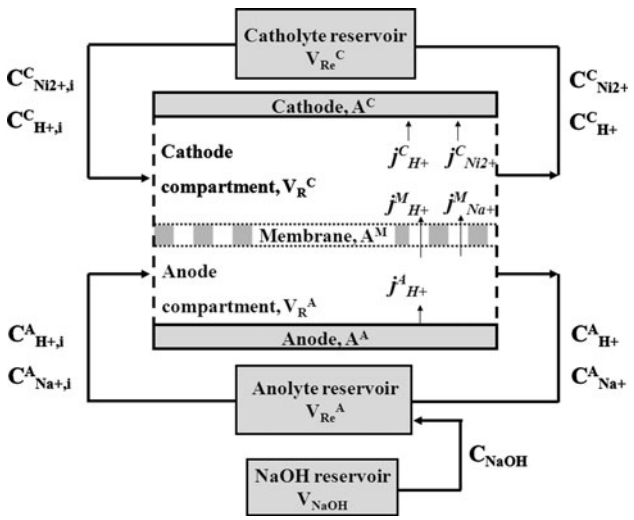

Fig. 2 Schematic of the flow circuit for an electrochemical reactor, operated in batch-recycle mode

7. Catholyte and anolyte temperatures are the same and time invariant.
8. Current is distributed uniformly over the electrodes, which were assumed to be equipotential surfaces.

A set of charge and mass balances on relevant species were used to describe the operation of the nickel recovery reactor at a macroscopic scale. The relationship between the fluxes of H^+ and Na^+ ions through the membrane is defined approximately by Eq. (37). In Eqs. (37–43), V and A represent volume (m^3) and area (m^2), respectively; subscripts/superscripts C, A and M refer to cathode/catholyte, anode/anolyte and membrane processes, respectively.

$$j_{M,Na^+} \cdot [H^+]_A \approx \frac{D_{Na^+}}{D_{H^+}} \cdot j_{M,H^+} \cdot [Na^+]_A \tag{37}$$

As the sole anode reaction (17) produces protons, the ratio $[Na^+]/[H^+]$ in the anolyte will decrease with time in batch systems, leading eventually to the flux through the membrane being dominated by protons, thereby decreasing the catholyte pH and hence the charge yield for nickel deposition. To mitigate this effect, continuous additions of NaOH to the anolyte were modelled to assess the effect on the catholyte pH of neutralising the protons in the anolyte, while replenishing the sodium ions depleted by the flux through the membrane from anolyte to catholyte. The mass balance equations on protons and sodium ions in the anolyte are given in (38) and (39), respectively.

$$V_A \frac{d[H^+]_A}{dt} = \frac{j_{A,H^+} \cdot A_A}{F} - \frac{j_{M,H^+} \cdot A_M}{F} - \frac{dV_{NaOH}}{dt} \cdot [NaOH] \tag{38}$$

$$V_A \frac{d[Na^+]_A}{dt} = -\frac{j_{M,Na^+} \cdot A_M}{F} + \frac{dV_{NaOH}}{dt} \cdot [NaOH] \tag{39}$$

The mass balances on H^+ and Ni^{II} in the catholyte are:

$$V_C \frac{d[H^+]_C}{dt} = -\frac{j_{C,H_2} \cdot A_C}{F} + \frac{j_{M,H^+} \cdot A_M}{F} \tag{40}$$

$$V_C \frac{d[Ni^{II}]_C}{dt} = -\frac{j_{C,Ni} \cdot A_C}{2F} \tag{41}$$

Finally, the electro-osmotic drag coefficients representing the number of H_2O molecules passing through the membrane with each H^+ and Na^+ ion: ξ_{H_2O,H^+} and ξ_{H_2O,Na^+} respectively, were used to calculate the temporal change in anolyte and catholyte volumes, according to (42) and (43), respectively:

$$V_A(t) = V_A(0) + \frac{dV_{NaOH}}{dt} \cdot t - \frac{M_{H_2O}}{\rho_{H_2O}} \left(\xi_{H^+} \frac{j_{M,H^+} A_M}{F} + \xi_{Na^+} \frac{j_{M,Na^+} A_M}{F} \right) \cdot t \cdot 10^{-6} \tag{42}$$

$$V_C(t) = V_C(0) + \frac{M_{H_2O}}{\rho_{H_2O}} \left(\xi_{H^+} \frac{j_{M,H^+} A_M}{F} + \xi_{Na^+} \frac{j_{M,Na^+} A_M}{F} \right) \cdot t \cdot 10^{-6} \tag{43}$$

where $V(t)$ and $V(0)$ represent electrolyte volumes at times t and $t = 0$, respectively. This allowed for the decrease in Ni^{II} concentration in the catholyte due to dilution, as well as depletion by electrochemical reduction.

Coupling of the micro-kinetic cathode model and macro-kinetic reactor model was achieved by substituting the equations for j_{Ni} and j_{H_2}, derived in the micro-kinetic model, into $j_{C,Ni}$ and j_{C,H_2} in the catholyte mass balances in the reactor model. Provided that the concentrations of all species are specified in the reactor model at $t = 0$ and that the dependence of all kinetic rate coefficients on $[Ni^{II}]$ and $[H^+]$ are included in the reactor model, the combined model may be used to predict reactor performance data, including charge yields, as functions of experimental variables such as solution flow rates and rates of NaOH addition to the anolyte.

3 Experimental

3.1 Determination of micro-kinetics

A rotating disc electrode (RDE) was made from a 6.25 mm diameter Ni disc (99.995 %, Alfa Aesar) embedded in a 22 mm diameter PTFE sheath, the rotation rate of which was controlled by a motor/controller (Pine Instrument Company, Raleigh, NC, USA). A Pt/Ti mesh counter electrode and a saturated calomel reference electrode (SCE) (Cole-Parmer, UK) were used in a three compartment glass cell for determination of the electrochemical reduction kinetics for Ni^{II}, H^+ and H_2O with a Metrohm PGSTAT 30 Autolab potentiostat/galvanostat.

The RDE was polished mechanically on a polishing machine (Buehler), using 300 nm followed by 50 nm particle diameter Al_2O_3 powder in water, followed by rinsing of the disc with a jet of ultrapure water. The electrode was immersed in an ultrasonic bath for 15–20 min following the polishing procedure and finally rinsed again with ultrapure water prior to immersion in the electrolyte.

All synthetic electrolyte solutions were prepared from analytical grade chemicals (Sigma Aldrich) and high purity water, made by reverse osmosis (Elga Elgastat Prima) and de-ionisation (Elga Elgastat Maxima). The compositions of electrolytes, made with analytical grade chemicals, are listed in Table 2.

H_2 evolution kinetics were recorded in solutions (i) and (ii) in the pH range 2.0–4.0 in the absence and the presence of 190 mol m^{-3} of $B(OH)_3$, while applying a negative-

Table 2 Composition of electrolytes used in kinetic studies on a Ni RDE

Solution code	Na_2SO_4 (mol m^{-3})	NH_3SO_3 (mol m^{-3})	$B(OH)_3$ (mol m^{-3})	$Ni(NH_2SO_3)_2{\cdot}4H_2O$ (mol m^{-3})
i	500	250	–	–
ii	500	250	190	–
iii	500	230	190	10
iv	500	50	190	100

going linear potential sweep from potentials of zero current down to −1.2 V (SCE) at a scan rate of 10 mV s^{-1}, evoking (pseudo-) steady state currents [25]. Ni^{II} reduction kinetics were determined in solutions (iii) and (iv) containing $B(OH)_3$ in the presence of 10 and 100 mol m^{-3} of $Ni(NH_2SO_3)_2{\cdot}4H_2O$ in the pH range 2.0–4.0 using a cyclic voltammetry procedure. Solution pH was adjusted using either NH_3SO_3 or NaOH. All solutions contained 500 mol m^{-3} of Na_2SO_4 as supporting electrolyte and the concentration of sulfamic acid was kept constant in all solutions. Measurements on the Ni RDE were made at 540, 960 and 1,500 RPM. Bulk solution pH was monitored in situ during each experiment with a pH electrode and meter (Hanna Instruments Ltd., UK). Prior to and during all kinetic measurements, the solution was purged with high purity N_2 gas (Domnick Hunter NG104 N_2 generator). All data were recorded at a temperature of ca. 23 °C and each set of measurements was repeated several times to ensure reproducibility.

A Metrohm/Autolab electrochemical quartz crystal microbalance (EQCM) module with an Au/TiO_2 coated AT-cut quartz crystal of 3.5×10^{-5} m^2 area was used in conjunction with the PGSTAT 30 Autolab potentiostat to estimate nickel charge yield, Φ^e_{Ni}, as a function of electrode potential using the change in the electrode mass due to Ni deposition, as predicted by the Sauerbray Equation [26]:

$$\Delta m = -C_f \cdot \Delta f \tag{44}$$

where C_f is the sensitivity coefficient (4.29 ng Hz^{-1}) of the particular quartz crystal employed and Δf is the change in the frequency of the crystal oscillation caused by mass variations in the electrode. Measurements were conducted in solution (iv) at bulk pH 3.0 in the absence of convective mass transport. The upper potential limit in the cyclic scans was extended to +0.3 V (SCE) to establish the noise levels in the frequency response of the EQCM prior to nickel deposition.

3.2 Reactor experiments

Electrochemical recovery of nickel from industrial effluents was investigated under constant current control in a custom built electrochemical reactor [27] made from PMMA. Figure 3 shows the schematic of the reactor compartment structures and flow circuits. The reactor incorporated a 0.04×0.2 m^2 Ni mesh cathode (total surface area ca. 8×10^{-3} m^2), a 0.05×0.2 m^2 Ti/Ta_2O_5–IrO_2 (total surface area ca. 1.4×10^{-2} m^2) mesh anode and a Nafion 424 cation-permeable membrane (DuPont Inc.) and was operated in batch-recycle mode. Both reactor compartments accommodated SCE reference electrodes (Cole-Palmer), connected with the electrodes by narrow flow channels. Electrolytes were circulated with DC-powered, magnetically coupled centrifugal pumps (Pan World Co. Ltd) through the reactor compartments, cross-sectional areas being 4×10^{-4} and 1.25×10^{-2} m^2 for catholyte and anolyte, respectively. The catholyte flow rate was measured with a micro-turbine flow meter (Titan Enterprise) incorporated into the flow circuit.

A nickel sulfamate effluent sample containing 2×10^3 mol Ni^{II} m^{-3} was employed as the catholyte; 10^3 mol Na_2SO_4 m^{-3} solution was used as anolyte in the nickel recovery experiments. A HP 8452A UV–visible spectrophotometer (Agilent Technologies UK Ltd) was used to monitor Ni^{II} concentrations by measuring the Ni^{II} absorption peak heights at 393 nm. The nickel mesh cathode was weighed at regular time intervals and the mass accumulation was used to evaluate Φ^e_{Ni}. These charge yields were compared with those values obtained from measured changes in Ni^{II} concentrations. Anolyte and catholyte pHs were monitored continuously.

The effect of catholyte pH on the nickel(II) reduction charge yield was investigated in the absence and the presence of pH control, achieved by continuous addition of 4.4×10^3 mol NaOH m^{-3} to the anolyte with the aid of a peristaltic dosing pump (Ismatec). This was done to maintain a high $[Na^+]$ to $[H^+]$ ratio in the anolyte, thereby decreasing the H^+ transference number through the membrane and preventing the decrease in catholyte pH which typically leads to reduced Φ^e_{Ni}.

3.2.1 *Prediction of mass transport rates*

Recovery of nickel at constant current, $I_{Applied}$, requires an accurate prediction of the temporal change in the mass transport limited Ni^{II} reduction current, I_{Lim}, since excess current drives the hydrogen evolution loss reaction when $I_{Applied} > I_{Lim}$. To enable the evaluation of I_{Lim} with

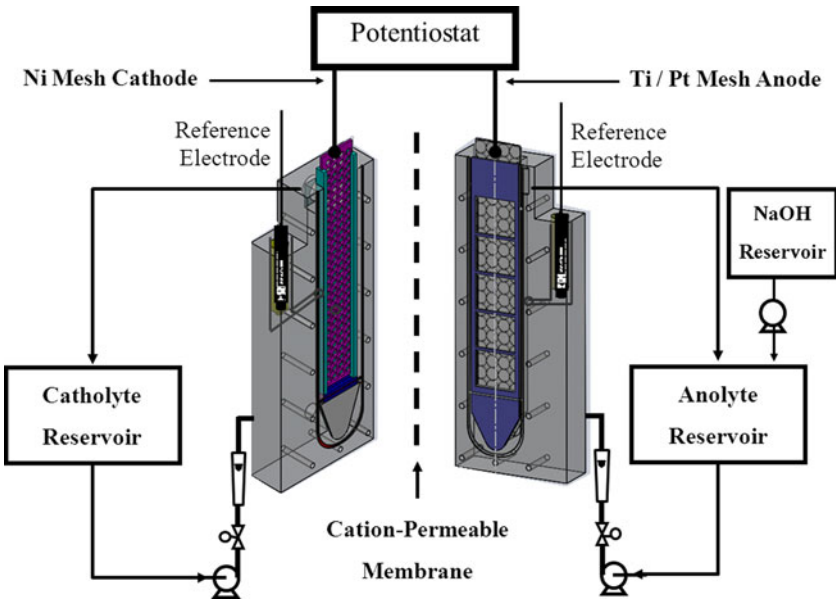

Fig. 3 Schematic of flow circuit and electrochemical reactor, operated in batch-recycle mode

changing Ni^{II} concentration in the reactor, the products of mass transport rate coefficients at mesh electrodes, k_m, and the nickel mesh cathode face area, A, were determined experimentally as a function of catholyte flow rate using the mass transport controlled reduction of hexacyanoferrate(III) ions in the reactor system described above. Solution volume of 5×10^{-4} m^3 containing 10^2 mol $K_3[Fe(CN)_6]$ m^{-3} and 10^3 mol Na_2CO_3 m^{-3} as supporting electrolyte at pH 10 were circulated through the cathode compartment. The charge passed to reduce $Fe(CN)_6^{3-}$ to $Fe(CN)_6^{4-}$ was measured at various flow rates at a potential of -0.85 V (SCE), and the corresponding k_mA were evaluated:

$$Q_i = t \cdot k_m A \cdot c_i \cdot v_e F \tag{45}$$

where Q, t, k_m, A, c_i, and v_e denote charge passed to reduce species i, time, mass transport rate coefficient, cathode surface area, concentration of species i and electron stoichiometry of the reduction reaction.

4 Results and discussion

4.1 Experimental kinetics of Ni^{II}, H^+ and H_2O reduction

4.1.1 Hydrogen evolution kinetics in the absence of Ni^{II}

The kinetics of H_2 evolution on a Ni RDE were studied in sulfate–sulfamate media in the absence and the presence of $B(OH)_3$ in the pH range 2.0–4.0. Figure 4 shows the kinetics measured in the absence of $B(OH)_3$ during linear potential sweeps at 10 mV s^{-1} from potentials of zero current down to -1.2 V (SCE). The $\ln(|j|)$ data are presented as a function of the hydrogen overpotential.

The regions of kinetic, mixed and mass transport controlled rates of H^+ reduction are evident in Fig. 4. As expected, the kinetically controlled currents at low overpotentials were invariant with proton concentration. In the mixed control regions, the plots of $\ln(|j|)$ versus η_{H^+/H_2} showed an increase in magnitudes of the measured currents with decreasing pH. The plots did not exhibit linear gradients characterised by an overall Tafel coefficient. Furthermore, it is notable that the gradients of the $\ln(|j|)$ versus η_{H^+/H_2} curves changed more rapidly in the transition region between mixed and mass transport controlled kinetics as the bulk pH was increased. The onset of H_2O reduction was not evident at potentials less negative than -1.2 V (SCE). Finally, $B(OH)_3$ exhibited no effect on the H_2 evolution kinetics, contrary to results reported [28] for non-sulfamate solutions.

4.1.2 Kinetics in the presence of Ni^{II}

Figures 5 and 6 show the kinetics of simultaneous H_2 evolution and nickel(II) reduction on a Ni RDE in sulfate–sulfamate solutions with $B(OH)_3$ and 10 or 100 mol Ni^{II} m^{-3}, respectively, in the pH range 2.0–4.0. The $\ln(|j|)$ data are plotted as a function of the hydrogen overpotential at each pH to enable the evaluation of the effect of H^+ concentration on the kinetics of nickel(II) reduction.

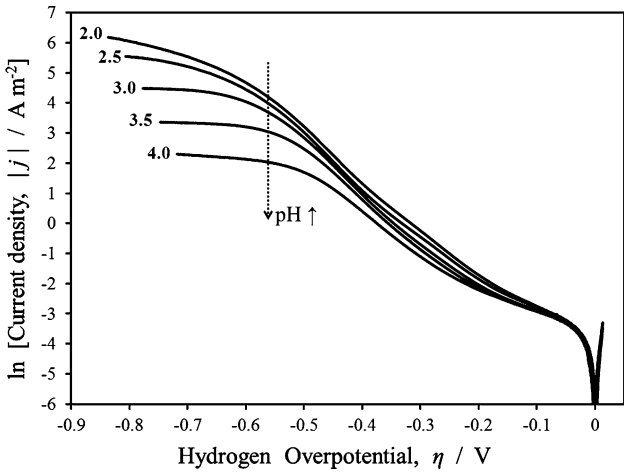

Fig. 4 H^+/H_2O reduction kinetics measured in the pH range 2.0–4.0 in solutions containing 500 mol Na_2SO_4 m^{-3} and 250 mol NH_3SO_3 m^{-3} at a Ni RDE rotating at 1,500 RPM

Figures 5 and 6 show that the data measured at bulk pH 3.0, 3.5 and 4.0 displayed nearly identical linear gradients in the low overpotential regions. The linear regions of the curves measured at these pH were used to determine the Tafel slopes, evaluated between hydrogen overpotentials of −0.12 and −0.40 V, as 205 mV dec^{-1} in 100 mol Ni^{II} m^{-3} and 212 mV dec^{-1} in 10 mol Ni^{II} m^{-3} solution.

Figures 7 and 8 show the effects of adding 10 and 100 mol Ni^{II} m^{-3} on $\ln(|j|)$—η_{H^+/H_2} data for bulk solution pH 2.5 and 3.5, respectively. In the solution of pH 3.5, for which, as shown in Figs. 5 and 6, the competition from the hydrogen evolution reaction was less significant, the kinetics of nickel(II) reduction from solutions of 10 and

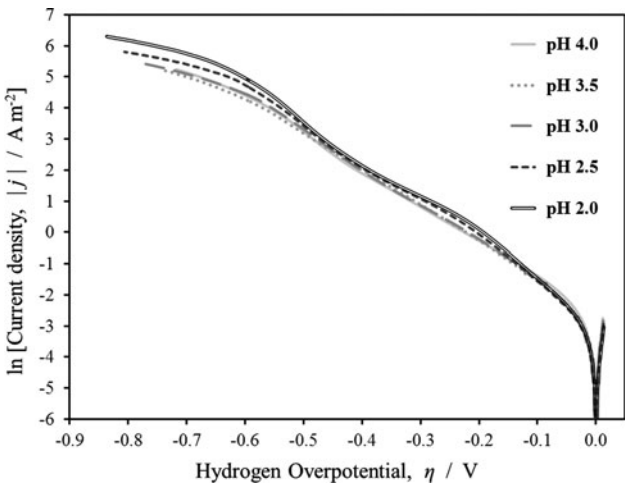

Fig. 5 H^+/H_2O and nickel(II) reduction kinetics measured in the pH range 2.0–4.0 in solutions containing 500 mol Na_2SO_4 m^{-3}, 250 mol NH_3SO_3 m^{-3}, 190 mol m^{-3} $B(OH)_3$ and 100 mol Ni^{II} m^{-3} at a Ni RDE rotating at 1,500 RPM

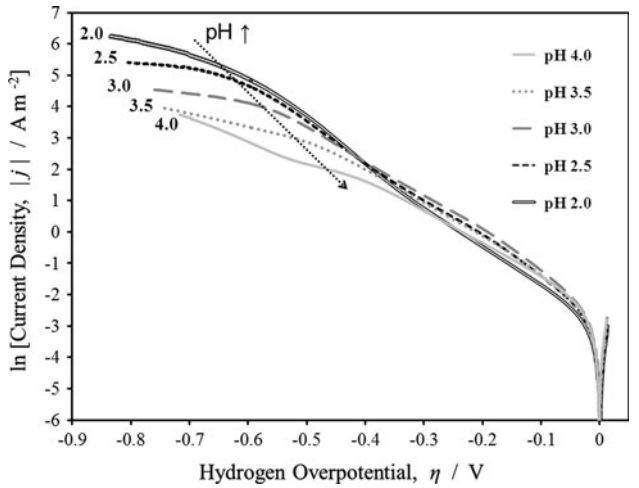

Fig. 6 H^+/H_2O and nickel(II) reduction kinetics measured in the pH range 2.0–4.0 in solutions containing 500 mol Na_2SO_4 m^{-3}, 250 mol NH_3SO_3 m^{-3}, 190 mol m^{-3} $B(OH)_3$ and 10 mol Ni^{II} m^{-3} at a Ni RDE rotating at 1,500 RPM

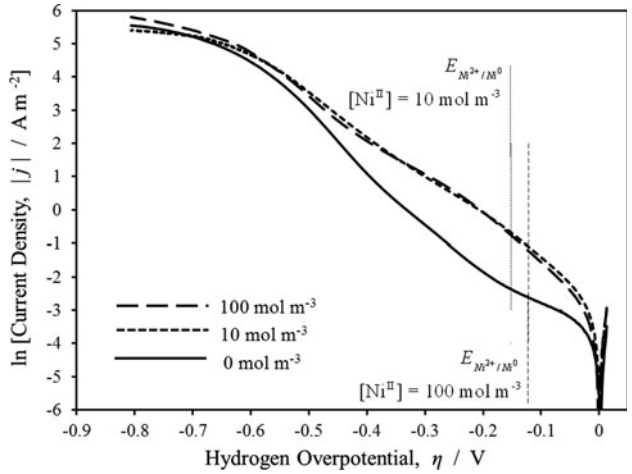

Fig. 7 H^+/H_2O and nickel(II) reduction kinetics measured in pH 2.5 solutions containing 500 mol Na_2SO_4 m^{-3}, 250 mol NH_3SO_3 m^{-3}, 190 mol m^{-3} $B(OH)_3$ and (i) 0 mol Ni^{II} m^{-3}, (ii) 10 mol Ni^{II} m^{-3} and (iii) 100 mol Ni^{II} m^{-3}measured at a Ni RDE rotating at 1,500 RPM

100 mol Ni^{II} m^{-3} were essentially the same, except in the mass transport controlled region. In the solution of bulk pH 2.5, the data measured in the presence of 10 and 100 mol Ni^{II} m^{-3} were essentially indistinguishable, even at higher overpotentials when the mass transport limited nickel(II) reduction currents were obscured by H^+ reduction currents. It is noteworthy that current densities in the region $E_{Ni^{2+}/Ni^0} \leq E \leq E_{H^+/H_2}$ were consistently greater in the presence of nickel(II) than in its absence over the pH range $2.5 \leq pH_{bulk} \leq 4.0$. This cannot be explained by the reduction of nickel(II), since that would be expected to be occur only at $E \leq E_{Ni^{2+}/Ni^0}$.

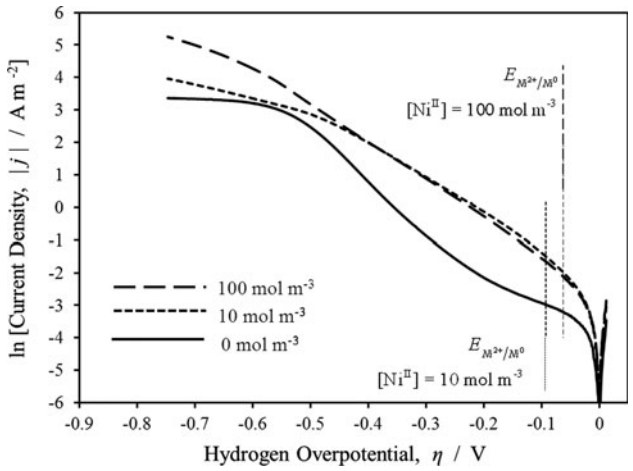

Fig. 8 H^+/H_2O and nickel(II) reduction kinetics measured in pH 3.5 solutions containing 500 mol Na_2SO_4 m^{-3}, 250 mol NH_3SO_3 m^{-3}, 190 mol m^{-3} $B(OH)_3$ and (i) 0 mol Ni^{II} m^{-3}, (ii) 10 mol Ni^{II} m^{-3} and (iii) 100 mol Ni^{II} m^{-3}measured at a Ni RDE rotating at 1,500 RPM

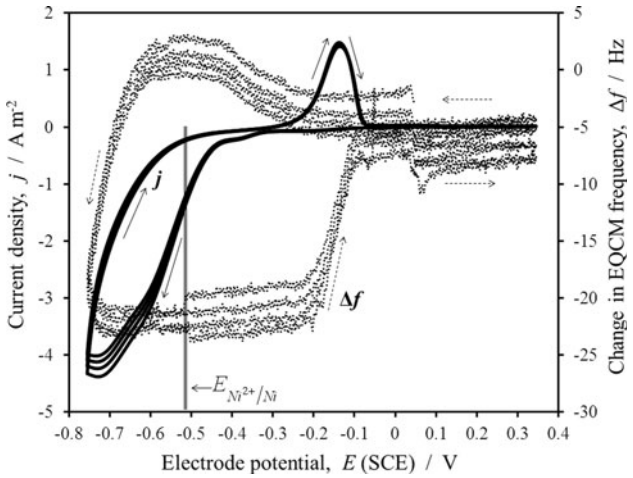

Fig. 9 EQCM response (*dotted line*) during potential cycling (*solid line*) of Au electrode in 100 mol Ni^{II} m^{-3}, 500 mol Na_2SO_4 m^{-3}, 250 mol NH_3SO_3 m^{-3} and 190 mol m^{-3} $B(OH)_3$ at pH 3.0

Figure 9 shows the frequency response of an Au-coated quartz crystal to potential cycling in a solution containing 100 mol Ni^{II} m^{-3} at pH 3.0. The frequency response indicated that Ni deposition occurred at potentials < ca. −0.65 V (SCE), which is negative of the equilibrium potential for the Ni^{2+}/Ni^0 couple (−0.515 V (SCE) at 100 mol Ni^{II} m^{-3}) by ca. 0.13 V, confirming that the additional currents measured in the potential region $E_{Ni^{2+}/Ni^0} \leq E \leq E_{H^+/H_2}$ were not due to the reduction of nickel(II). Furthermore, it should be noted that on the positive-going scans, the frequency change corresponding to dissolution was evident at more positive potentials than those at which oxidation current densities occurred. It is proposed that the initial oxidation current corresponded to the oxidation of Ni^0–Ni^I and that additional overpotential was required for its dissolution as Ni^{II}; only the latter process would result in the positive frequency change detected.

4.2 Model fitting and predictions of micro-kinetics

The current densities recorded in the kinetic experiments were modelled using the kinetic Eqs. (20–36), in which the unknown kinetic rate coefficients and transfer coefficients were derived using gPROMS software (www.psenterprise.com). Parameters were obtained by iterative fitting processes with an imposed maximum constant variance of 0.1 between experimentally determined values of the total current density and the model fit. Values of the transfer coefficients α_i were treated as unknown quantities in all individual electron transfer rate equations for nickel(II) and proton reduction reactions.

A constraint range was imposed on each parameter. For the transfer coefficients, α, the imposed boundary conditions were $0.1 \leq \alpha_i \leq 0.9$; for the kinetic rate coefficients, k, the constraint range was typically $10^{-13} \leq k_i \leq 10^5$. An 'initial guess' was also assigned to each parameter: 0.5 for α and 10^{-3} for k_i.

4.2.1 Proton reduction kinetics

The micro-kinetic model in Eqs. (20–26), (32) and (34) was fitted to the hydrogen evolution current densities as a function of the hydrogen overpotential. There were altogether six unknown parameters: k_{V_c}, k_{V_a}, k_{H_c}, k_T, α_V and α_H. These kinetic rate coefficients and transfer coefficients were obtained to describe the experimental measurements made in solutions of bulk pH 2.5, 3.0, 3.5 and 4.0 at an RDE rotation rate of 1,500 RPM. Data obtained in pH 2.0 solution was not modelled due to possible effects from the chemical dissociation of NH_3SO_3 ($K = 0.1$ [29]) and HSO_4^- ($K = 0.01$ [7]) on mass transport limited current densities. For the Volmer reaction step [Eq. (21)], the mass transport rate coefficient for H^+ ions of 4.2×10^{-4} m s^{-1} was imposed, evaluated using the H^+ diffusion coefficient of 1.27 ($\pm$0.07) $\times$ 10^{-8} m^2 s^{-1} and computed from the measured mass transport limited current densities at rotation rates of 540, 960 and 1,500 RPM in the pH range 3.0–4.0. The maximum surface coverage by adsorbed H atoms, $\Gamma_{H,max}$, was assumed to be limited by the atomic surface density of the underlying substrate, $\Gamma_{Ni,max}$. The value of 2.16×10^{-5} mol m^{-2} for $\Gamma_{Ni,max}$ was computed based on the atomic nickel radius of 1.49 Å and fractional 2D packing density of 0.91. The determined kinetic parameters are shown in Table 3.

The proposed dependence of the kinetic rate coefficients and transfer coefficients on bulk pH is shown in Eqs. (46–51). While the cathodic rate coefficient, k_{V_c}, for the Volmer reaction was found to increase exponentially with increasing pH, the product $k_{V_c} \times [H^+]$ was found to exhibit a linear increase

Table 3 Kinetic parameters representing the evolution of H_2 on Ni via the combined Volmer–Heyrovsky–Tafel mechanism, as determined using gPROMS

pH	k_{V_c} (m s^{-1})	$k_{V_c} \times [H^+]$ (mol m^{-2} s^{-1})	k_{V_a} s^{-1}	k_{H_c} (m s^{-1})	$k_{H_c} \times [H^+]$ (mol m^{-2} s^{-1})	k_T/s^{-1}	α_V	α_H
Parameters								
2.5	15.4	48.7	65.8	2.44×10^{-9}	7.72×10^{-9}	3.61×10^{-2}	0.56	0.49
3.0	42.0	42.0	19.4	6.93×10^{-9}	6.93×10^{-9}	3.61×10^{-2}	0.51	0.49
3.5	110.0	34.8	11.9	1.80×10^{-8}	5.70×10^{-9}	3.61×10^{-2}	0.47	0.49
4.0	275.0	27.5	2.87	4.21×10^{-8}	4.21×10^{-9}	3.61×10^{-2}	0.42	0.49

pH	k_{V_c} (m s^{-1})	k_{V_a} (s^{-1})	k_{H_c} (m s^{-1})	k_T (s^{-1})	α_V	α_H
95 % confidence intervals						
2.5	2.9×10^{-10}	2.8	5.2×10^{-11}	6.1×10^{-4}	8.6×10^{-3}	Value fixed
3.0	7.3×10^{-7}	8.6	1.2×10^{-10}	1.1×10^{-4}	2.1×10^{-3}	Value fixed
3.5	5.3×10^{-7}	2.1	6.2×10^{-10}	3.5×10^{-4}	2.6×10^{-3}	Value fixed
4.0	1.3×10^{-5}	5.1	9.1×10^{-9}	7.7×10^{-3}	1.4×10^{-2}	Value fixed

Underlined confidence intervals are those which exceed the corresponding parameter value and are therefore less reliable

with decreasing pH. This correctly reflects the increase in the magnitudes of the experimentally measured current densities with decreasing pH in the mixed control regions. Likewise, the product $k_{H_c} \times [H^+]$ was found to increase with decreasing pH approximately linearly. As expected, the rate coefficient for the Tafel recombination step was constant throughout the pH range at 3.61×10^{-2} s^{-1}, giving the product $k_T \times \Gamma_{H,max}$ of 7.80×10^{-7} mol m^{-2} s^{-1}.Over the pH range investigated, it was found that $k_{H_c} \times [H^+] \ll k_T \times \Gamma_{H,max} \ll k_{V_c} \times [H^+]$, showing that the Heyrovsky step was rate determining. While the transfer coefficient for the Heyrovsky step could be maintained at a constant value of 0.49, the coefficient for the Volmer step was found to decrease slightly with increasing pH.

$$k_{V_c} = 1.29 \times 10^{-1} \exp\{1.92 \times \text{pH}\} \quad (46)$$

$$k_{V_a} = 8.90 \times 10^{3} \exp\{-1.98 \times \text{pH}\} \quad (47)$$

$$k_{H_c} = 2.22 \times 10^{-11} \exp\{1.90 \times \text{pH}\} \quad (48)$$

$$k_T = 3.61 \times 10^{-2} \quad (49)$$

$$\alpha_T = -9.20 \times 10^{-2}\text{pH} + 7.89 \times 10^{-1} \quad (50)$$

$$\alpha_H = 0.49 \quad (51)$$

Figure 10 compares experimental data and the curves computed using the parameter trends in Eqs. (46–51), together with the dependence of the fractional surface coverage by adsorbed hydrogen, θ_H, on overpotential and pH.

4.2.2 Nickel(II) reduction kinetics

The micro-kinetic model representing hydrogen evolution kinetics on Ni was extended to include Eqs. (27–31), (33), (35) and (36), representing the reduction of nickel(II).

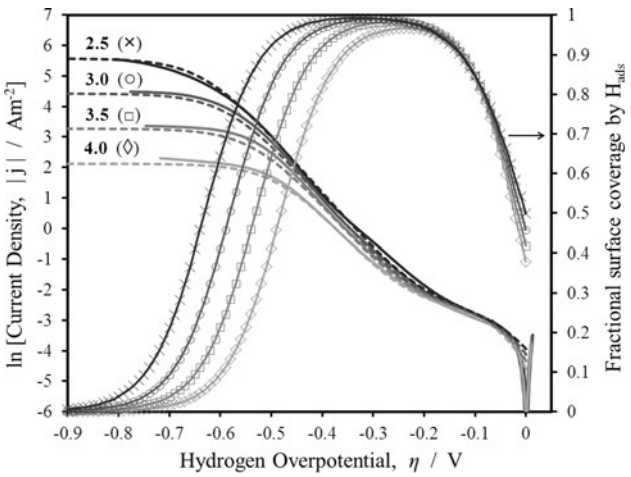

Fig. 10 Comparison between (*thick straight line*) experimental data and (*spaced hyphen*) model predictions for H_2 evolution on Ni at pH 2.5–4.0

Equations (46–51), representing the kinetic rate coefficients for the hydrogen evolution reaction, were included and assumed not to be affected by the presence of nickel(II). Three kinetic rate coefficients and two transfer coefficients representing the reduction of nickel(II) in Eqs. (27–31), (33): $k_{Ni,c1}$, $k_{Ni,a1}$, $k_{Ni,c2}$, $\alpha_{Ni,1}$ and $\alpha_{Ni,2}$ were estimated using experimental data obtained for 10 and 100 mol Ni^{II} m^{-3} at bulk pHs 2.5, 3.0. 3.5 and 4.0 at an RDE rotation rate of 1,500 RPM. Evaluated using the Ni^{2+} diffusion coefficient of 6.61×10^{-10} m^2 s^{-1} [16], the mass transport rate coefficient of 5.9×10^{-5} m s^{-1} was imposed on the first electron transfer [Eq. (28)] in nickel(II) reduction. $\Gamma_{Ni,max}$ was taken to be 2.16×10^{-5} mol m^{-2}.

The observed increase in the current densities in the potential range $E_{Ni^{2+}/Ni^0} \leq E \leq E_{H^+/H_2}$ in the presence of nickel(II) in solution could not be explained using the mechanism proposed in (27–31). It is possible that a form of catalysis, whereby the adsorption of H_{ads} is catalysed by Ni^I_{ads}, takes places via reaction (52), as has been suggested previously [15].

$$Ni^I_{ads} + H^+ + e^- \rightarrow Ni^I_{ads} + H_{ads} \quad (52)$$

Ni^I_{ads} is likely to be present on the electrode surface at the onset of the proton reduction reaction when the electrode potential is applied in a cyclic manner, as was determined from the measurements with the electrochemical crystal microbalance. However, the inclusion of this mechanism introduces additional unknown parameters into the micro-kinetic model and while the probability of a better match with experimental data would be possible, the reliability of the parameter output values would be decreased greatly. Moreover, the correct method of inclusion of catalysis is not unambiguous.

In the absence of reliable kinetic equations that could account for the increased currents at low hydrogen over-potentials in the presence of nickel(II), the model was fitted to experimental data with a focus on maximising the fit at higher overpotentials. It is arguable that high deposition rates are desirable during nickel(II) recovery and so a good fit at high overpotentials is of more technological importance than at low overpotentials.

Table 4 lists the kinetic rate and transfer coefficients that were determined to represent the reduction of nickel(II) at concentrations of 10 and 100 mol m^{-3} in the pH range 2.5–4.0. Only the cathodic rate coefficient for the first electron transfer, $k_{Ni,c1}$, exhibited clear concentration dependence, as shown in (53); the remaining parameters were invariant with Ni^{II} concentration.

$$k_{Ni,c1} = 1.10 \times 10^{-7} \exp\left\{-2.30 \times 10^{-3} \cdot [Ni^{II}]\right\} \quad (53)$$

An example of the partial nickel(II) and proton reduction current densities are shown in Fig. 11 for a solution of bulk pH 3.5 containing 100 mol Ni^{II} m^{-3}. While the modelled partial Ni^{II} reduction current densities clearly represent only a limited section of the experimentally determined reduction curves, the kinetic parameters determined using gPROMS were nonetheless employed to examine the principle of using micro-kinetic trends to predict macro-kinetic results.

The parameter trends presented in Eqs. (46–51) and (53) and the nickel(II) concentration invariant parameters presented in Table 4 were used to compute a set of nickel(II) reduction charge yield curves as a function of nickel(II) concentration, bulk solution pH and the hydrogen overpotential. The results, shown in Fig. 12, were projected up to Ni^{II} concentrations of 10^3 mol m^{-3}. It is shown that the sensitivity of the nickel charge yield to solution pH is much greater than its sensitivity to Ni^{II} concentration.

It is evident that it is desirable to maintain the solution pH at values above 2.5 in order to achieve high charge yields, which could be maintained at above 0.9 at nickel(II) concentrations above 10^2 mol m^{-3}. The peaks in the charge yield values present at hydrogen overpotentials of ca. −0.2 V, reflect the maximum divergence between the currents measured in the absence and the presence of nickel(II) (Figs. 7, 8). It should be noted that Fig. 12 indicates non-zero nickel(II) charge yields at $\eta_{H^+/H_2} = 0$ V at nickel(II) concentrations of 10^2–10^3 mol m^{-3} at bulk pH

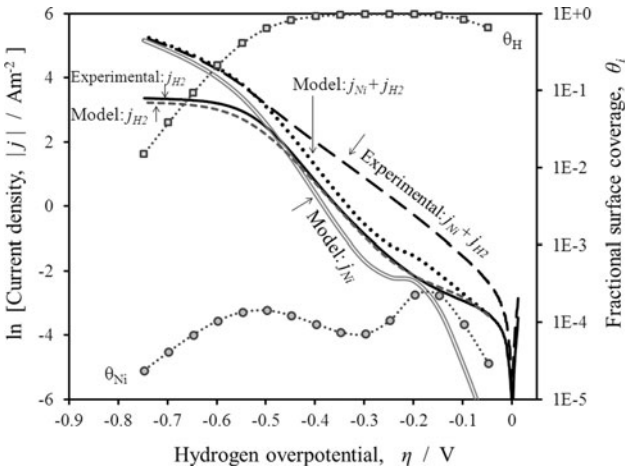

Fig. 11 Comparison between experimental data and model predictions for nickel(II) reduction and H_2 evolution on Ni in the presence of 100 mol Ni^{II} m^{-3} at bulk pH 3.5

Table 4 Kinetic parameters representing the reduction of nickel(II), as determined using gPROMS

Ni^{II} (mol m^{-3})	$k_{Ni,c1}$ (m s^{-1})	$k_{Ni,c1} \times [Ni^{2+}]$ (mol m^{-2} s^{-1})	$k_{Ni,a1}$ (s^{-1})	$k_{Ni,c2}$ (m s^{-1})	$\alpha_{Ni,1}$	$\alpha_{Ni,2}$
Parameters						
10	1.65×10^{-7}	1.65×10^{-6}	2.73×10^{3}	9.40	0.18	0.456
100	8.75×10^{-8}	8.75×10^{-6}	2.74×10^{3}	9.40	0.18	0.456
95 % confidence intervals						
For both concentrations	8.3×10^{-10}	–	1.1	0.52	4.50×10^{-5}	Value fixed

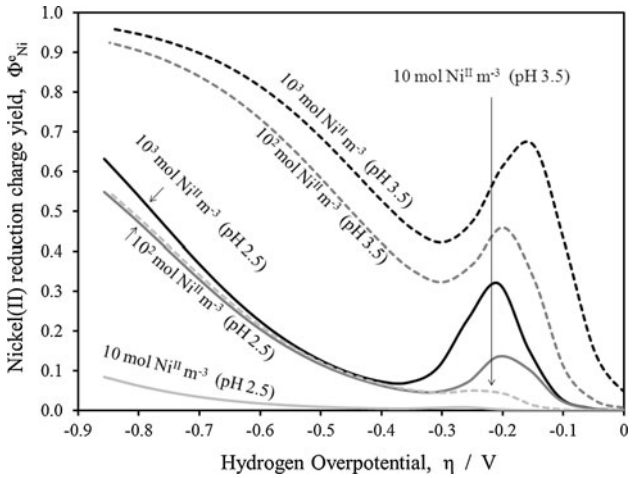

Fig. 12 Nickel(II) reduction charge yields computed as a function of the hydrogen overpotential from kinetic parameters for 10, 10^2 and 10^3 mol Ni^{II} m^{-3} at pHs 2.5 and 3.5

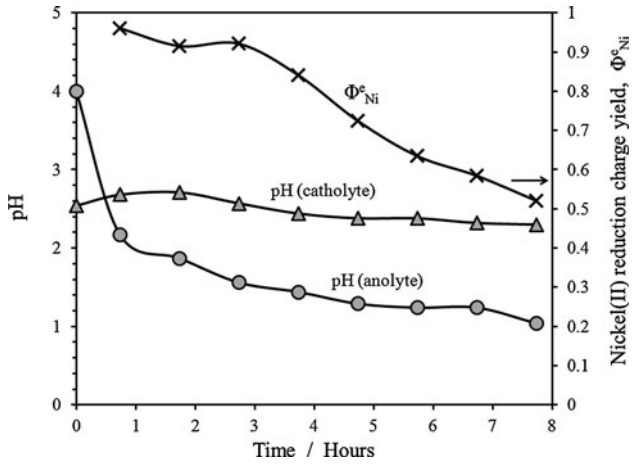

Fig. 13 Time dependence of pHs and nickel charge yield during treatment of an effluent containing 2×10^3 mol Ni^{II} m^{-3} at an applied current of 5 A (ca. 625 A m^{-2}) in the absence of NaOH additions

3.5. Given the equilibrium potentials for the nickel(II) and proton reduction reactions in Eqs. (13) and (14), nickel(II) reduction should not be energetically favourable to proton reduction at bulk pH $\leq$ 3.5. The predicted early onset of nickel(II) reduction is hence a consequence of the model maximising its fit with the experimental data. Since the kinetic rate coefficients for the hydrogen evolution reaction were fixed, the kinetic rate coefficients for the nickel(II) reduction process were computed by the model to account for the increased currents at low hydrogen overpotentials in the presence of nickel(II). Given the results obtained on the EQCM, this may be an erroneous representation of the processes occurring at low hydrogen overpotentials and so the construction of a more complete model should be the subject of further investigation.

4.3 Electrochemical reactor performance

Initially, a nickel sulfamate effluent sample containing 2×10^3 mol Ni^{II} m^{-3} was processed in the reactor at a constant current of 5 A (ca. 625 A m^{-2}) in the absence of anolyte pH adjustments. The linear flow rate of the catholyte through the cathode compartment of the reactor was fixed at 2.2×10^{-2} m s^{-1} (Re $\approx$ 350). Such an applied current was expected to exceed the mass transport limited value only after 10 h of reactor operation, provided nickel(II) was reduced continuously with a charge yield of unity.

As shown in Fig. 13, the experimentally determined charge yield was calculated to remain above 0.9 only for the first 3 h of reactor operation, decreasing thereafter linearly by 0.05 U h^{-1} to a value of 0.52 at 8 h. This decrease in the charge yield coincided with a decrease in catholyte pH to values below 2.5. This is consistent with the conclusions drawn from Fig. 12.

Between one and 2 h of reactor operation, the catholyte pH passed through a maximum. At the initial anolyte pH of 4.0, the ratio of Na^+:H^+ anolyte concentrations and fluxes were 10^4 and 1.05×10^3, respectively, resulting in an initial increase in catholyte pH as the protons consumed at the cathode were not replenished by protons from the anolyte. However, the flux ratio decreased with time as the sodium ions were depleted and the protons, generated by reaction (17) at the anode, became the primary carriers of current through the membrane.

4.3.1 Model fitting and predictions for reactor control

Equations (37–43) of the reactor-scale model were solved in gPROMS simultaneously with Eqs. (20–36) of the micro-kinetic model to determine the control parameters for the second experiment conducted with pH adjustments. The boundary conditions at $t = 0$ s input into the model were (i) the concentration of nickel(II) in the catholyte (2×10^3 mol m^{-3}), (ii) the catholyte–effluent pH (2.5), (iii) the anolyte pH (2.4), (iv) the concentration of Na^+ in the anolyte (10^3 mol m^{-3}), (v) the catholyte volume (6×10^{-4} m^3) and (vi) the anolyte volume (10^{-3} m^3). The current across the electrochemical cell was fixed at a value of 5 A (ca. 625 A m^{-2} at the cathode). The rate of addition of 4.4×10^3 mol NaOH m^{-3} to the anolyte was fixed at 1.12×10^{-8} m^3 s^{-1} in order to maintain a constant flux ratio between Na^+ ($D_{Na^+} = 1.33 \times 10^{-9}$ m^2 s^{-1} [28]) and H^+ ions through the membrane assuming a constant Φ^e_{Ni} of ca. 0.95. The electro-osmotic drag coefficients ξ_{H_2O,H^+} and ξ_{H_2O,Na^+} were assigned values of 2.6 and 7, respectively [30].

The experimentally determined catholyte and anolyte pH values, as well as the nickel(II) reduction charge yields,

which were calculated based on mass accumulation on the cathode, are compared with their respective model predictions in Fig. 14. These results demonstrated improved stability in catholyte and anolyte pHs and charge yields with pH adjustments. At the imposed NaOH feed rate, the anolyte pH was expected to decrease from its starting value of 2.5 to a constant value of 2.12, as shown in Fig. 14, and the fluxes of H^+ and Na^+ and ions through the membrane were predicted to remain constant at ca. 9.3×10^{-4} and 1.8×10^{-2} mol m^{-2} s^{-1}, respectively. Experimental measurements of anolyte pH showed that it remained stable throughout the duration of the experiment. For up to 3 h of reactor operation, the anolyte pH remained precisely at a value of 2.11, subsequently undergoing a sudden decrease to a value of 1.95, at which it remained fairly stable for the remaining 4 h. These results indicate that the relative fluxes of protons and sodium ions through the membrane were maintained at fairly constant values with the aid of NaOH additions. The additions of NaOH also successfully prevented the catholyte pH from decreasing relative to its starting value and thereby the nickel(II) reduction charge yield was maintained at an average value of 0.94 ± 0.03 throughout the duration of the experiment, as shown in Fig. 14. The slower than predicted increase in catholyte pH to a stable plateau at pH 3.38 was caused presumably by a minor offset in the rate of dosing by the peristaltic pump.

The temporal depletion in nickel(II) concentration, determined from the UV absorbance at 393 nm, is compared in Fig. 15 with values obtained from measurements of electrode mass using Eq. (54):

$$[\mathrm{Ni^{II}}](t_2) = \left([\mathrm{Ni^{II}}](t_1) - \frac{(m_c(t_2) - m_c(t_1))}{V_c(t_1)}\right)\frac{V_c(t_1)}{V_c(t_2)} \quad (54)$$

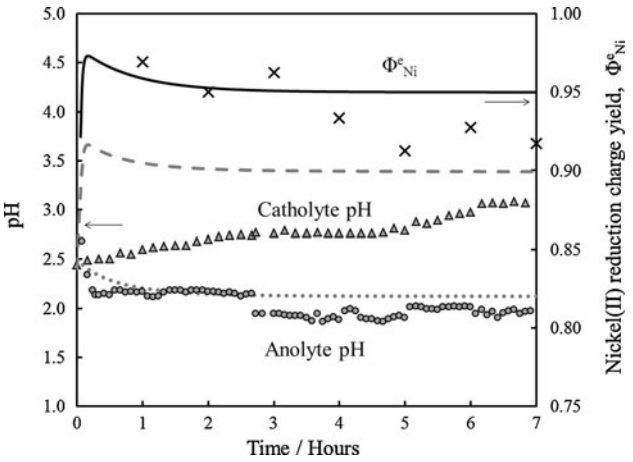

Fig. 14 Time dependences of catholyte and anolyte pHs: (*filled triangle*) and (*filled circle*) represent the measured catholyte and anolyte pH, respectively; (*spaced hyphen*) and (*doted line*) are predicted catholyte and anolyte pHs, respectively. Ni^{II} reduction charge yields: (*cross*) determined from changes in electrode mass and (*thick straight line*) model prediction

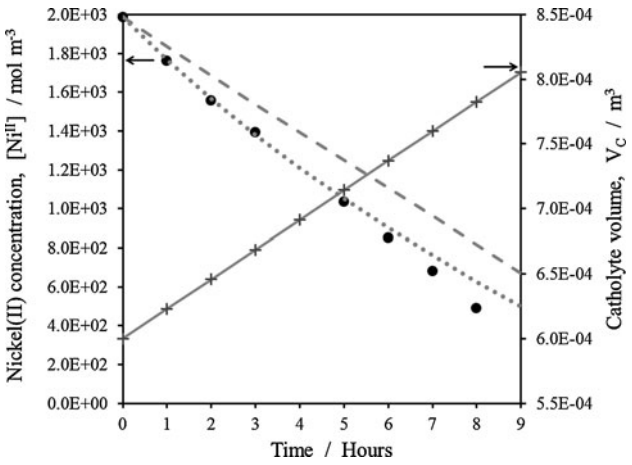

Fig. 15 Temporal depletion of Ni^{II} at 5 A (ca. 625 A m^{-2}): (*filled square*) experimental data determined using absorbance measurements at 393 nm; (*doted line*) and (*spaced hyphen*) are model predictions based on inclusion and exclusion of electro-osmotic transport of H_2O through membrane, respectively. (*Plus*) is the computed temporal increase in catholyte volume

where V_C and m_C are the catholyte volume and cathode mass, respectively, and t_1 denotes values corresponding to an earlier time than t_2. The change in catholyte volume with time was computed using the reactor model in which the electro-osmotic transport of H_2O molecules through the membrane was taken into account using Eq. (43). The computed $[Ni^{II}]$ concentrations are also shown for the case when the catholyte volume was assumed to remain constant at its initial value. Figure 15 demonstrates that the inclusion of electro-osmotic effects in the macro-kinetic model greatly decreased the discrepancy between the Ni^{II} concentration values measured by UV absorbance and electrode weight and is thus a mandatory feature of the reactor model.

5 Conclusions

Designed for nickel recovery from nickel sulfamate effluents, a membrane-separated electrochemical reactor was operated at constant current in batch-recycle mode, and incorporated a nickel mesh cathode, $Ti/Ta_2O_5–IrO_2$ mesh anode and cation-permeable membrane to prevent anodic oxidation of sulfamate. The decrease in the nickel charge yield below 0.9 with time resulted primarily from the time-dependent decrease in catholyte pH, due to anodic oxygen evolution causing the proton flux through the membrane to increase with time.

A model combining the micro-kinetic expressions with the mass and charge balances on the reactor was used successfully to determine the rate of NaOH additions to the anolyte, decreasing the flux of H^+ through the membrane

and thereby permitting nickel(II) recovery with an average charge yield of 0.94.

In the micro-kinetic model, the processes of nickel(II) and proton reduction in sulfamate solutions were treated as two multi-step reactions involving adsorbed intermediates, Ni^{I}_{ads} and H_{ads}, respectively. The unknown kinetic parameters were obtained successfully using *gPROMS* software by iterative fitting of the model to experimental data obtained over a range of Ni^{II} concentrations and bulk solution pH, enabling evaluation of nickel(II) reduction charge yields as functions of nickel(II) concentration, pH and electrode potential. Although additional modelling is required to describe the mechanism of nickel reduction in sulfamate solutions adequately, a combination of micro-scale and macro-scale kinetic models has been shown to produce acceptable predictions of reactor performance.

Acknowledgments The authors thank the UK Engineering and Physical Sciences Research Council and Atranova Ltd. for an Industrial CASE studentship for A.K.

References

1. Dannenberg EM, Paguin L (2007) Kirk-Othmer encyclopedia of chemical technology. Wiley, New York
2. Huang C-H (1994) Plat Surf Finish 8:64
3. Lin CS, Hsu PC, Chang L, Chen CH (2001) J Appl Electrochem 31:925
4. Saitou M, Oshiro S, Asadul Hossain SM (2008) J Appl Electrochem 38:309
5. Goods SG, Kelly JJ, Talin AA, Michael JR, Watson RM (2006) J Electrochem Soc 153:C325
6. Wagman DD, Evans WH, Parker VB, Schumm RH, Halow I, Bailey SM, Churney KL, Nuttall RL (1982) J Phys Chem Ref Data 11(Suppl 2):2
7. Schmid GM (1985) Standard potentials in aqueous solutions. In: Bard AJ, Parsons R, Jordan J (eds) IUPAC. Marcel Dekker: New York
8. Tilak BV, Gendron AS, Moisoiu MA (1977) J Appl Electrochem 7:495
9. Marti J (1966) Plating 53:61
10. Klingenmeier O (1965) Plating 52:1138
11. Greene A (1968) Plating 55:594
12. Zhang H, Park S-M (1994) J Appl Electrochem 24:1182
13. Novikov LG, Kurnoskin GA, Flerov VN, Shulygin GP, Ivashkina IU (1989) Zashch Met 25:871
14. Bockris JO, Drazic D, Despic A (1961) Electrochim Acta 4:325
15. Epelboin I, Jousselin M, Wiart R (1981) J Electrochem Soc 119:61
16. Vazquez-Arenas J, Pritzker MD (2010) J Electrochem Soc 157:D283
17. Dahms H, Croll I (1965) J Electrochem Soc 112:771
18. Hessami S, Tobias C (1989) J Electrochem Soc 136:3611
19. Holm M, O'Keefe T (2000) J Appl Electrochem 30:1125
20. Horkans J (1979) J Electrochem Soc 126:1861
21. Deligianni H, Romankiw L (1993) IMB J Res Dev 37:85
22. Tsuru Y, Nomura M, Foulkes F (2002) J Appl Electrochem 32:629
23. Hoare J (1987) J Electrochem Soc 134:3102
24. Walker ATS, Wragg A (1977) Electrochim Acta 22:1129
25. Bockris J, Reddy A, Gamboa-Aldeco M (eds) (2000) Modern Electrochemistry 2A: fundamentals of electrodics. 2nd edn. Kluwer Academic/Plenum Publishers, New York
26. Buttry DA, Ward MD (1992) Chem Rev 92:1355
27. Kelsall GH, Kovaleva A (2010) ECS Trans 28(6): 317
28. Zech N, Landolt D (2000) Electrochim Acta 45:3461
29. Kurtz J, Farrar J (1969) J Am Chem Soc 91:6057
30. Breslau BR, Miller IF (1971) Ind Eng Chem Fundam 10:554